

Laser Patterning Assisted Devitrification and Domain Engineering of Amorphous and Nanocrystalline Alloys

Ahmed Talaat^{1,*}, David W. Greve^{2,3}, Alex Leary⁴, Yuzhe Liu¹, Jörg Wiezorek¹, Paul R. Ohodnicki, Jr ^{1,5}

¹Mechanical Engineering & Materials Science, Swanson School of Engineering, University of Pittsburgh, Pittsburgh, PA, 15261, USA

²DWGreve Consulting, Sedona, AZ, 86351, USA

³Electrical & Computer Engineering, Carnegie Mellon University, Pittsburgh, PA, 15213, USA

⁴Materials and Structures Division, NASA Glenn Research Center, Cleveland, OH, 44135, USA

⁵Electrical & Computer Engineering, Swanson School of Engineering, University of Pittsburgh, Pittsburgh, PA, 15261, USA

(*) Corresponding e-mail: AHT17@pitt.edu

Abstract

We have investigated laser-patterning and devitrification as a novel method to realize emergent properties in modified regions at the ribbon surface consisting of periodic localized laser spots thermally treated under rapid heating and cooling conditions. Fe-based amorphous ribbons were annealed for systematically varied laser power. Extremely high heating and cooling rates on the order of 10^8 - 10^{10} K/s have been estimated by finite element analysis simulations. Observations suggest surface melting followed by rapid solidification fast enough to quench and form an amorphous structure upon cooling. Diffusion of heat occurs from the laser irradiated surface region so that a finite volume of material surrounding this region rises in temperature above the crystallization temperature relevant for conventional isothermal annealing experiments. The underlying mechanism of laser annealing and consequences of heat transients involved are discussed in terms of impacts upon micro/nanostructure, residual stresses, and magnetic domain structure surrounding the laser irradiated region. The study illustrates the potential to exploit spatially optimized phase transformations in a scalable manufacturing process of amorphous and nanocrystalline alloys to locally access otherwise inaccessible extreme heating and cooling rates.

Keywords: Amorphous Ribbons, Laser Processing, Nanocrystallization, Rapid Annealing, Magnetic Domains.

1. Introduction

Crystallization from an amorphous precursor is exploited to synthesize metastable soft magnetic nanocomposite systems of transition metal rich ferromagnetic nanocrystals embedded in an intergranular amorphous phase. First, rapid solidification processing with cooling rates of $\sim 10^6$ K/s in selected complex alloy chemistries enables synthesis of an amorphous precursor^{1–3}. Subsequent thermal processing steps produce highly refined microstructure with nm-scale grain sizes to enable effective exchange averaging and highly reversible magnetization processes as described by the random anisotropy model⁴. FeSiNbBCu-based “Finemet” alloys originally invented by Yoshizawa et al.⁵ represent the first class of commercial alloys. Superior soft magnetic properties in this alloy system results from ubiquitous nucleation and self-limiting growth of nanocrystals due to expulsion of glass formers to the intergranular amorphous matrix, requiring significant metalloids and early transition metals to reduce effective saturation magnetization.

Recent work demonstrates the balance between nucleation and growth can alternatively be optimized through highly controlled thermal processing of amorphous precursors with extremely rapid heating and subsequent cooling rates on order of 10^2 – 10^3 K/s referred to as “flash annealing”, with a high density of nucleation sites achieved for limited nanocrystal growth even for alloy chemistries which do not produce nm-scale microstructures with conventional annealing^{6,7}. Unprecedented combinations of high saturation magnetization and low losses are realized through flash annealing of alloy chemistries with substantially reduced metalloid and early transition metal element glass formers and diffusion inhibitors. High heating and cooling rates generated during laser radiation offered great advantages for rapid thermal processing of various families of magnetic materials⁸ and surface treatment of ferromagnetic amorphous ribbons^{9,10}.

From a manufacturing perspective, reel-to-reel strain annealing methods (also referred to as in-line methods) have been recently employed, showing great promise for precise control of

magnetic properties with additional benefits for scalability^{11,12}. Although flash annealing methods have demonstrated significant material property performance improvements at laboratory scale, there are inherent technical challenges for scaling to a manufacturing environment. In-line methods are compatible with electromagnetic field assisted processing methods with the additional advantage of spatially selective heating which may be possible through techniques such as laser annealing². In this work, we report on pulsed-laser processing of Fe-based amorphous ribbons with emphasis placed on spatially varying thermal history and spatial profile within the laser-irradiated regions as well as impacts on surrounding regions due to the detailed thermal effects associated with the laser pulse. We discuss impacts on phase transformations, residual stresses, and magnetic domain structure, motivating concepts of laser patterned micro- and domain structure engineering.

2. Experimental Techniques

Amorphous ribbons with nominal composition $\text{Fe}_{73.5}\text{Si}_{15.5}\text{Nb}_3\text{B}_7\text{Cu}_1$ were used for laser experiments. Laser annealing was carried out using a Q-smart pulsed Nd-YAG (wavelength of 1064 nm) with laser beam diameter of ~0.6mm. Laser power was varied from 50-150 mJ and the time delay associated with each laser power was calculated using full-width-half-maximum (FWHM) of the laser output pulse. Microstructure and crystalline phases after laser annealing were characterized using x-ray diffraction, with an XRD Bruker D8 Discover Diffractometer with Cu-K radiation ($\lambda = 0.15418$ nm) and a slit size of 0.2 mm. Ribbon samples were attached to the diffractometer at which each scan was made over the two-theta angular range between 30-90° with a step size of 0.025° and scanning speed of 0.45°/sec. The length of irradiated area (L) on the sample was estimated from the height of the x-ray beam and the incident theta-2theta angular range (30-90°), to be on the order of 0.4-0.2 mm. X-ray point optics were also adjusted using a collimator with aperture of 1 mm to focus the beam on the irradiated laser spot. Scanning electron microscopy (SEM) analysis was performed using a Thermo Fisher Scientific Apreo SEM. Sample preparation

for transmission electron microscopy (TEM) was performed using dual-beam focused ion beam (FIB) FEI Scios system through lift-out techniques, with samples taken from the top ribbon surface at center and near edges of a laser irradiated region. TEM imaging was performed in bright-field and selected area diffraction modes using a JEOL JEM 2100F TEM. Magnetic domain images were observed by magneto-optical Kerr effect (MOKE) microscopy (Evico Magnetics GmbH).

3. Results and discussion

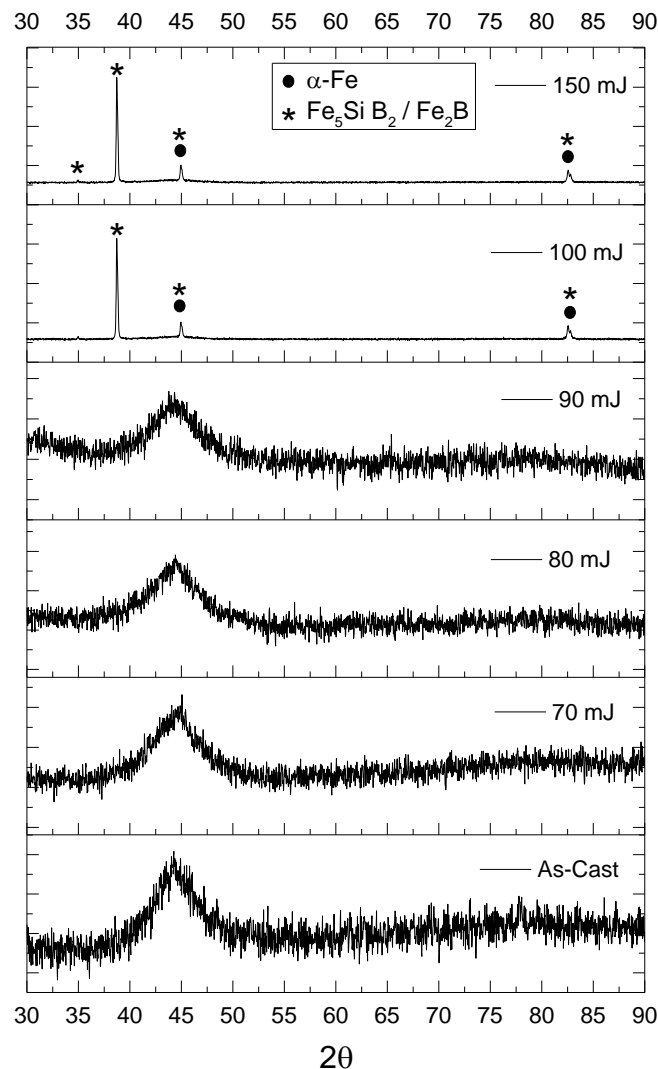


FIG. 1. XRD patterns of as-cast and laser-annealed Fe-based ribbons.

Fig. 1 shows XRD patterns of as-cast and laser annealed Fe-based ribbons at different laser power. Samples annealed at laser power level below 100 mJ remain fully amorphous, whereas

samples treated at higher laser power (i.e., $\geq 100\text{mJ}$) present XRD peaks indicative of the formation of nanocrystalline phases. For conventional annealing, the formation of primary nanocrystalline phases is followed by boride phases after reaching secondary crystallization temperatures as described in the following sequence ^{1,4}: Amorphous [$T < 500^\circ\text{C}$] \rightarrow amorphous + $\alpha\text{-Fe(Si)}$ [$510^\circ\text{C} < T < 590^\circ\text{C}$] \rightarrow Fe_2B / Fe_{23}B_6 [$T > 590^\circ\text{C}$]. These phase transformation temperatures are typically associated with characteristic times $> 1\text{s}$ and onset temperatures can be associated with activation energies through kinetics associated with heating rates. Laser processed ribbons do not show the conventional evolution of phases expected as a function of the increased pulsed laser intensity. As illustrated in **Fig. 1**, the observed crystalline phases can instead be indexed to body centered cubic $\alpha\text{-Fe}$ and boride-based intermetallic phases. Of particular note is the presence of a dominant peak at $2\theta \sim 38^\circ$ which, in combination with the additional peaks present, may be indicative of a dominant ternary intermetallic nominally identified as Fe_5SiB_2 , preferentially formed at the surface of the ribbons with a degree of crystallographic texture ¹³. We also note that the x-ray spot size on the sample surface is approximately $0.2\text{mm} \times 1\text{mm}$ in area centered within the laser irradiated spot of $\sim 0.6\text{mm}$ diameter, such that it spans beyond the irradiated laser spot processed region into the surrounding region impacted by thermal diffusion. Given the unique spatial and temporal profile characteristics of the thermal profile for pulsed laser irradiated samples, a need exists to revisit crystallization mechanisms considering detailed thermal histories experienced across and surrounding the laser pulse irradiated region.

During pulsed laser irradiation, the laser energy density decreases exponentially in the radial direction with a maximum at the laser spot center, leading to greater temperatures at the center and a temperature gradient from the center towards the irradiated area perimeter. In addition, the laser beam irradiation also produces a stress distribution associated with its Gaussian profile, developed within the residual tensile stress profile of the quenched ribbon produced during casting

¹⁴. Resulting inhomogeneous stress profiles are tensile at the center and compressive at the perimeter of irradiated areas ^{2,10}. Temporally and spatially dependent temperature and stress profiles can alter free volume, nucleation rate, and diffusion kinetics leading to rapid crystallization events and alternative pathways towards the crystalline phase. In addition, the relatively high energy density of the pulsed laser and short penetration depths into the amorphous ribbon can lead to exceedingly high temperatures on the top surface during initial irradiation. These unique thermo-physical effects upon laser interaction with amorphous ribbons can affect the evolution of phase transformations, including: (1) thermal ablation, (2) laser melting followed by rapid re-solidification, and (3) laser heating above the crystallization temperature of the amorphous alloy.

For the currently investigated samples, SEM images, e.g. **Fig. 2a**, show evidence for near-surface melting through the observed contrast which is consistent with slight surface deformation but without distorting the basic topography of the initial underlying sample surface, with the exception of the edge of the molten zone in which an accumulation of material can be observed. Estimated peak temperatures decrease as a function of distance from the center towards the edge of laser spots due to decreased laser intensity resulting in substantially different thermal profiles throughout the laser pulse irradiated region. According to finite element simulations described in more detail below, heating and cooling rates at the top surface can be on the order of 10^9 and 10^8 K/s; respectively, greater than cooling rates attainable through the rapid solidification processing during the planar flow casting of amorphous ribbons (10^5 - 10^6 K/s) ¹ as well as heating rates of laser annealed ribbons by means of continuous-wave laser processing (10^5 K/s) ^{2,10}. These exceptionally high heating and cooling rates are expected to severely restrict diffusion length scales. Finite element simulations also suggest the melting temperature of the amorphous ribbon can be exceeded during the initial laser pulse irradiation at the top surface, such that melting at the surface followed by rapid solidification fast enough to quench to an amorphous solid appears feasible. The presence

of amorphous structure for the top surface of the ribbon both near edges and at the center of the laser irradiated region has been confirmed by selected area diffraction and TEM imaging, consistent with this assertion (**Fig. 2b-c**). For surrounding regions below the top surface and surrounding the primary laser irradiation region, substantially reduced peak temperatures below melting may instead yield devitrification with transformation pathways deviating from more conventional thermal processing due to residual stresses and exceptionally high heating rates.

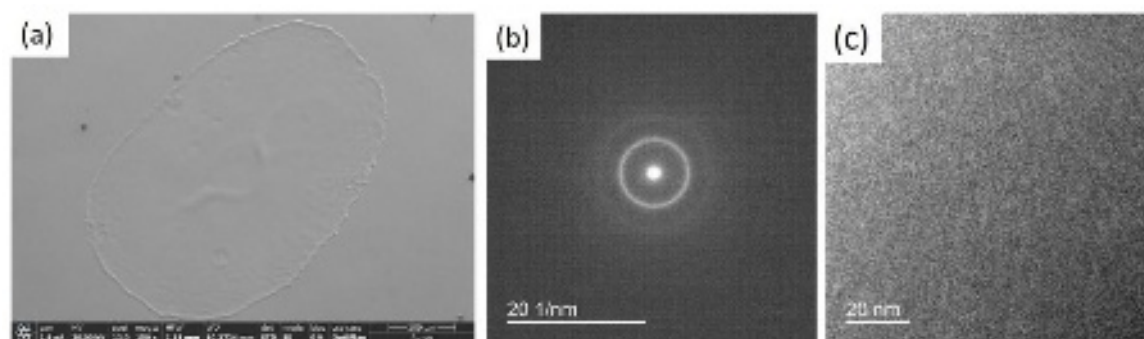


FIG. 2. (a) SEM micrograph of the ribbon surface layer showing evidence for local surface melting at the center of the laser irradiated region. (b) Selected area diffraction pattern showing an amorphous halo, and (c) bright field TEM image of laser annealed Finemet samples at 150 mJ at the top surface near the edges of the laser irradiated spot, showing a fully amorphous structure at the surface consistent with melting and rapid cooling.

Consistent with observations reported in **Fig. 2**, laser treatments of amorphous metals have been previously reported to result in surface melting and re-solidification without crystallization of the initial glassy structure due to the high cooling rates attained^{15–17}. However, solidification behavior of a surface-melted material is more complex than solidification developed during melt spinning or planar flow casting techniques used for the fabrication of magnetic amorphous ribbons. In the case of the pulsed laser processed samples, for which a local surface melting and re-solidification process has occurred, a tensile stress is expected near the center of the laser irradiated region while compressive stresses would be generated near the interface and surrounding the exterior of the direct laser irradiated region. Surface of the as-cast amorphous ribbons (**Fig. 3a**) shows a typical surface roughness consisting of slowly varying undulations on the length scale of ~50-100 microns in the plane and submicron to several microns vertically, typically observed for

the air side of as-cast amorphous ribbons¹⁸. After laser pulsing at laser power levels of 70-90mJ (**Fig. 3b-d**), an increased number of finer length scale undulations at the scale of several microns are observed on the sample surface in the irradiated regions and particularly localized around the outer diameter of the laser irradiated spot where compressive stresses would be dominant. Such features become more prominent upon increasing the laser power to 100-150 mJ (**Fig. 3e-f**), even showing evidence of tensile surface fractures at the laser irradiated spot center in some cases.

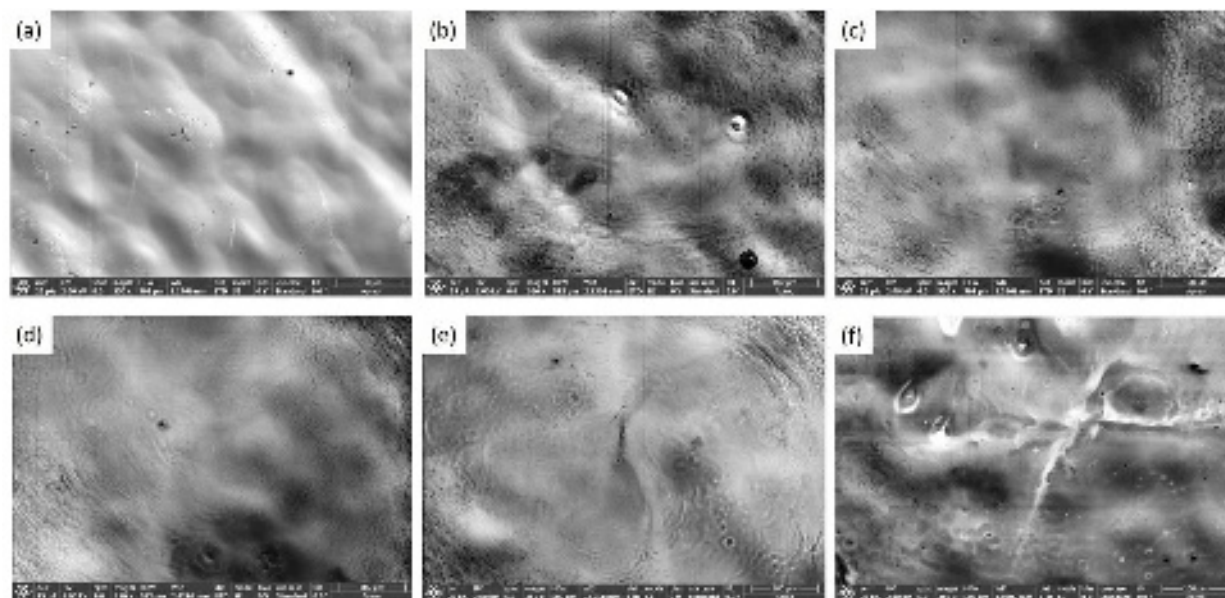


FIG. 3. SEM micrographs collected from the center of the laser irradiated spot of (a) as-cast and (b-f) laser annealed Fe-based ribbons at 70mJ, 80mJ, 90mJ, 100mJ, and 150mJ, respectively.

To gain further insights into the spatial and temporal evolution of the thermal history of the sample during pulsed laser irradiation, we have performed finite element simulations of the heat transfer. Material parameters used are taken from the published literature and are appropriate for representative Finemet amorphous alloys². A Finemet ribbon thickness of 15 micrometers was assumed along with a singular laser spot radius of 0.35 mm and a Gaussian laser pulse of total energy 100 mJ and duration of 3 ns. Simulations were performed using the heat transport module of COMSOL 5.6 for a cylindrically symmetric geometry and including conduction along with thermal radiation from both surfaces. For illustrative purposes, the heat of crystallization (186

J/(kg), exothermic) and melting (55 J/kg, endothermic) have also been included by adding temperature-dependent terms to the heat capacity to clarify potential impacts on the temporal and spatial thermal profile. Gaussian terms are added to an otherwise constant heat capacity to model these terms, with integrated areas corresponding to the heats of melting and crystallization. Simulation results are substantially dependent upon surface reflectivity and in the simulations presented here, a reflectivity of 0.9 was assumed representing the upper limit of reasonable values attainable. A peak surface temperature of more than 2000K is attained, and for reduced surface reflectivity values the peak temperature would be larger, consistent with predictions of a surface temperature high enough for surface melting and also with experimental results reported.

Fig. 4 shows the surface temperature at the laser spot center just below the surface (0.5 μ m) as a function of the logarithm of time. For $t < 20$ ns the temperature increases monotonically with time, with an increased slope at a temperature corresponding to exothermic crystallization, and with a ledge at a temperature corresponding to melting. The estimated maximum rate of change of temperature is extremely rapid ($\sim 10^{11}$ K/s), clearly indicating heating rates inaccessible with other techniques. The cooling rate at 0.5 μ m depth (approximately the penetration depth) below the surface is on order of 10^9 K/s, much faster than traditional rapid quenching techniques. Although potential impacts of the heat of transformation are modeled within the results of **Fig. 4**, these details do not dramatically impact predicted heating rates. For comparison, simulation results are also presented for several locations deeper within the ribbon ($\sim 7.5\mu$ m) and on the back ribbon surface ($\sim 15\mu$ m). Peak temperatures remain below melting but do reach typical primary crystallization and secondary crystallization temperatures, indicating that nanocrystallization may be possible.

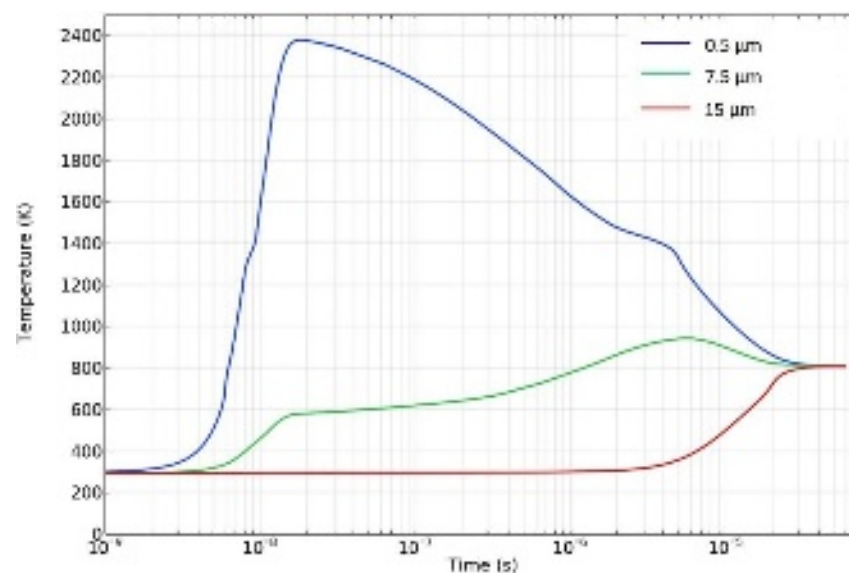


FIG. 4. Plot of temperature at the center of the laser spot on 0.5 μm as well as 7.5 μm below the surface, and 15 μm on the back ribbon surface as a function of time.

In addition to the variation in peak temperature throughout the thickness of the metallic ribbons, we can also consider the variation laterally on the top of the amorphous ribbon surface. For visualization purposes, we can illustrate the volume of the material that can potentially be “crystallized” and “melted” as illustrated in **Fig. 5** based upon peak temperature reached at a particular location and time by developing time – temperature profiles of the type illustrated in **Fig. 4**. For example, as shown in **Fig. 5a** at $t = 7.5$ ns (before the peak of the laser pulse) surface melting is possible within the laser irradiated spot size, surrounded by a larger surface ring of material still within the laser irradiated region only reaching temperatures corresponding to crystallization. At $t = 1$ μs (**Fig. 5b**), regions for which melting and crystallization temperatures are reached has been enlarged and region for which crystallized temperatures are reached has penetrated below the surface and extended slightly beyond the diameter of the original laser irradiation spot due to thermal diffusion. At $t = 40$ μs (**Fig. 5c**) the size of the region for which melting temperatures have been reached is largely unchanged and the region in which crystallization temperatures are attained extends through the entire layer thickness immediately beneath the irradiated surface. These simulations can be further understood based on heat transfer characteristics of the material and the

rate of heat transfer through thermal conduction. For example, the time required for a heat pulse on the top surface to reach half of the maximum value on the bottom surface is given by ¹⁹

$$t_{1/2} = 0.1388 \frac{\rho_m C_p d^2}{k} \quad (1)$$

where ρ_m is the mass density, C_p the heat capacity, d the layer thickness, and k the thermal conductivity. For this case the penetration time is 12.5 μs , far longer than the pulse length. As a result, the laser pulse establishes an initial surface temperature distribution above the melting temperature resulting in melting and re-solidification at rates that an amorphous surface layer is still retained, and without substantial thermal diffusion within the bulk of the amorphous ribbon. Following conclusion of the laser pulse, the heat then diffuses throughout the ribbon such that a volume of material surrounding the initial irradiated region can ultimately approach or exceed typical crystallization temperatures at exceedingly high heating rates. It is reasonable to expect spatially varying devitrification and formation of nanocrystalline phases which can also deviate from expectations for more conventional thermal processing conditions.

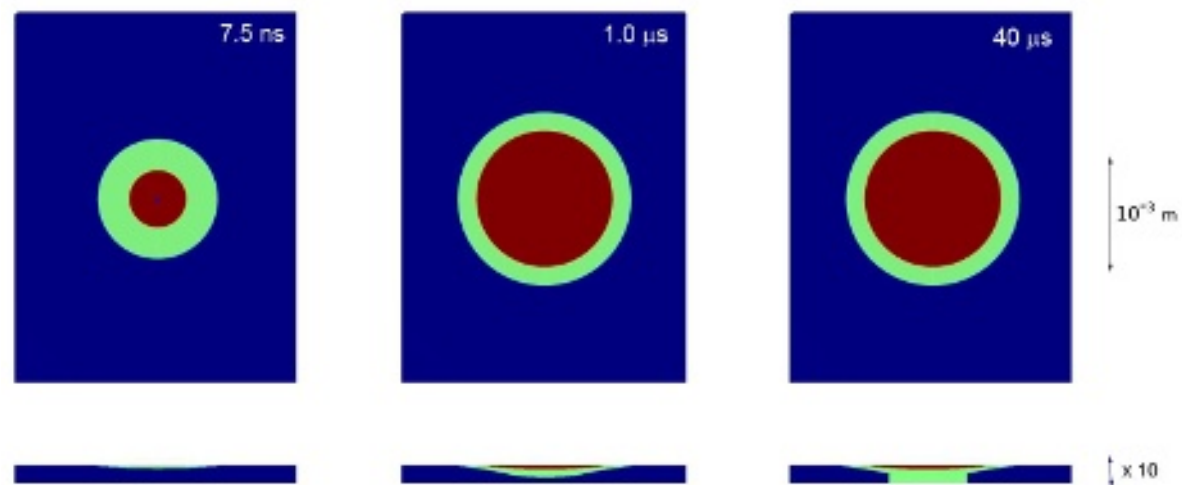


FIG. 5. FEA simulations of areas that have surpassed temperatures for which crystallization (green) and melting (red) is possible at a particular time and location. Regions indicated in green surpass crystallization temperatures and regions surpassing melting temperatures are indicated in red.

The crystallization of soft magnetic amorphous ribbons is typically assumed to be diffusion controlled, with a nucleation rate governed by both thermodynamic and kinetic aspects associated with atomic diffusion ^{2,20}. In traditional isothermal furnace annealing where heating rates are relatively slow (i.e., on the order of a few K/s) diffusion processes and structural relaxation of internal stresses induced following the production of amorphous ribbons through rapid solidification take place simultaneously upon annealing the amorphous precursor. The scenario is different in laser annealing where extremely high heating rates are involved along with localized thermal stresses which impact the amount of available free volume yielding modified kinetics ^{2,10}. Primary crystallization of amorphous metallic glasses occurs by two thermally activated processes, namely, nucleation and growth ²¹. Growth rates increase with increasing temperature below the melting temperature, whereas temperatures of maximum nucleation rate are attained in an intermediate range between melting and glass transition temperatures ^{1,22–24}. In Fe-based compositions, primary crystallization to a BCC or derivative phase is observed followed by the formation of boride based intermetallic phases at higher temperatures ²⁵. For flash annealing with high heating rates of $\sim 10^2$ - 10^3 K/s, nucleation rate has been proposed to be enhanced by rapid heating to temperatures approaching and above the glass transition temperature ^{2,24,26}. Modified kinetics resulting from the detailed thermal-mechanical state of the amorphous precursors as a function of time associated with pulsed laser processing can also potentially result in deviations from the expected primary and then secondary crystallization processes for standard annealing. Particularly due to top surface melting, chemical partitioning and enhanced kinetics immediately adjacent to the laser irradiated surface may exhibit substantially modified devitrification behavior requiring substantial further detailed study moving into the future.

In addition to spatially varying thermal profiles and associated phase transformations, induced residual stresses are expected within the surrounding amorphous ribbon for pulsed laser

processed ribbons. Residual compressive stresses can extend far beyond the irradiated region for regions of the sample in which the low peak temperatures achieved during thermal processing indicate that crystallization is not possible and will depend upon the detailed spatio-temporal thermal profile during laser irradiation as well as any phase transformations which occur during the subsequent thermal conduction. Depending upon the magnetostriction coefficient, residual stresses can also yield microscopic and macroscopic anisotropies due to the magnetoelastic coupling^{2,20}. Induced magnetoelastic anisotropies by means of local laser annealing associated with both compressive and tensile stresses allow for non-uniform stress distributions that can have a substantial impact on magnetic domain structure. **Fig. 6** shows magnetic domain images collected for laser annealed $\text{Co}_{74.6}\text{Fe}_{2.7}\text{Mn}_{2.7}\text{Nb}_4\text{B}_{14}\text{Si}_2$ Co-rich, $(\text{Fe}_{30}\text{Ni}_{70})_{80}\text{Nb}_4\text{Si}_2\text{B}_{14}$ Fe-Ni-rich, and $\text{Fe}_{73.5}\text{Si}_{15.5}\text{Nb}_3\text{B}_7\text{Cu}_1$ Finemet ribbons, respectively. Co-rich ribbons exhibit relatively narrow stripe domains due to the residual tensile stress in the as-cast ribbon and the small negative magnetostriction coefficient. Fe-based ribbons with a positive magnetostriction coefficient exhibit a network of domains running primarily parallel to the ribbon axis away from laser processed spots. Domain patterns inside spot regions show larger domains compared to as-cast regions, potentially due to nucleated Fe-Si grains with negative magnetostriction within the sample bulk thereby reducing magnetostriction coefficient. Laser annealing of Fe-Ni based alloy ribbons with relatively large positive magnetostriction ($\sim 18\text{-}23\text{ppm}$)^{27,28} shows clear impact on domain structures in surrounding regions. Specifically, Fe-Ni domains radiate outward from the laser spot following laser irradiation confirming residual compressive stresses. These observations demonstrate feasibility for periodic localized thermal-physical processing through pulsed laser methods to achieve spatially varied phase transformations and combined micro/domain structure engineering.

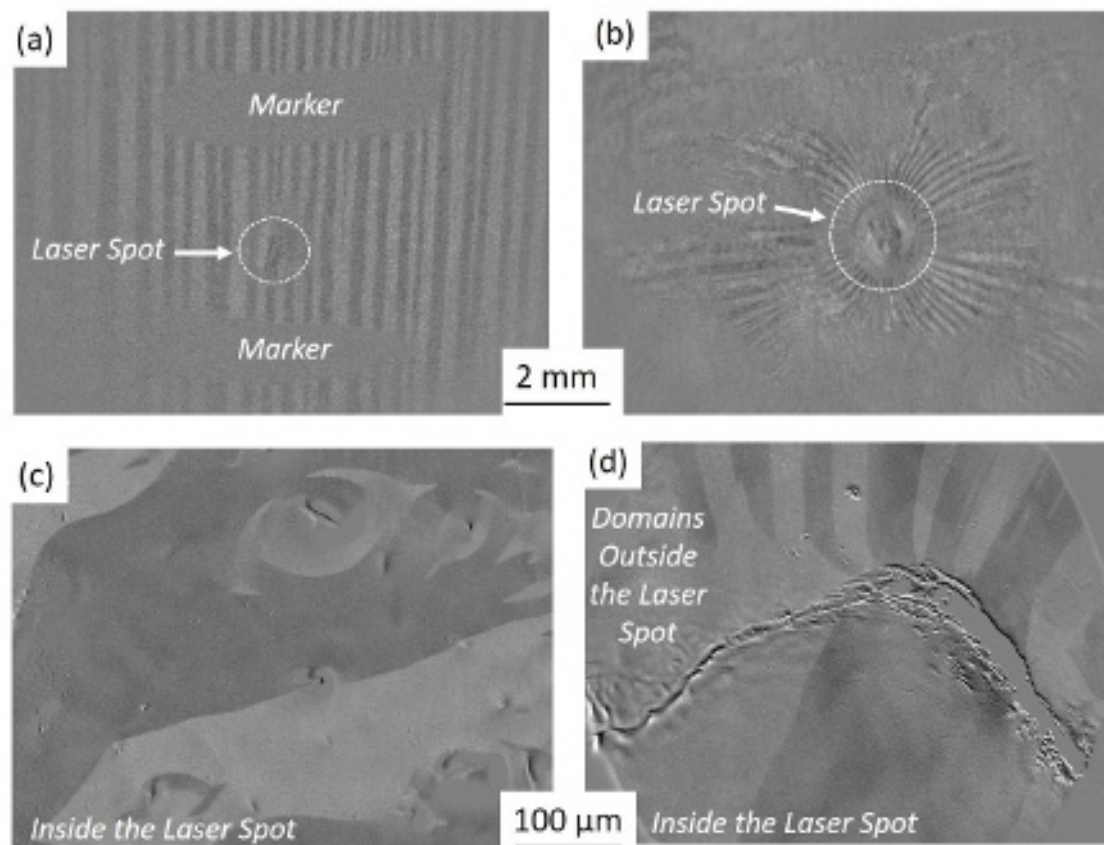


FIG. 6. Wide-view magnetic domain images of laser annealed (a) Co-rich ribbons and (b) Fe-Ni ribbons. Magnetic domain structure of laser annealed Finemet ribbons in the laser spot (c), and (d) domains outside the irradiated area.

4. Conclusions

In summary, we have investigated thermal processing of Fe-based amorphous ribbons by means of pulsed laser annealing for systematically varied laser power. Spatial and temporal evolution of the thermal profile upon laser annealing have been investigated, enabling unique phenomena to be observed within and surrounding the irradiated laser spot. Crystalline peaks of nanometer scale diameter have been observed above a critical laser power of 100mJ suggesting possibility of expected primary crystallization phases but also the formation of intermetallics. Based on finite element simulations, peak temperatures exceeding the melting temperature are expected at the top surface of ribbons, resulting in local surface melting within the irradiated region which can retain an amorphous structure upon re-solidification due to extremely rapid local

cooling. Through thermal diffusion from the laser irradiated surface region, reduced peak temperatures are observed throughout the ribbon depth and as a function of radial distance from the laser spot center which can nevertheless exceed the typical crystallization temperatures, resulting in the possibility of devitrification in the volume surrounding the laser irradiated spot. Compressive stresses are also induced within the surrounding amorphous region, at length scales much larger than the diameter of the spot resulting in modified domain structures due to induced magnetic anisotropies for magnetostrictive alloy systems. Through further investigation and optimization, laser processing represents a scalable manufacturing pathway and offers great opportunities for tailoring microstructures of amorphous and nanocrystalline alloys.

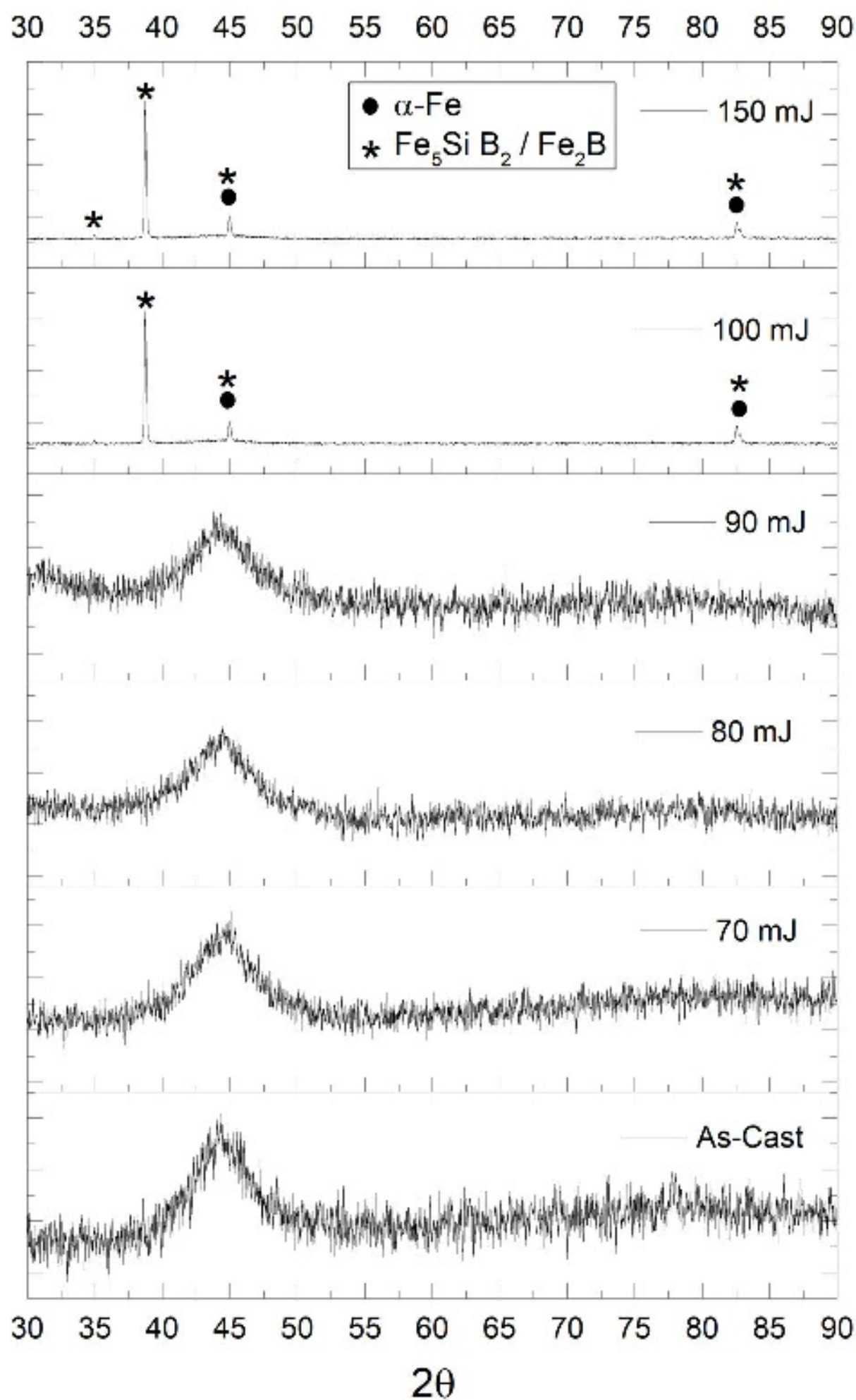
Acknowledgments

The authors acknowledge financial support from the University of Pittsburgh Dean's Office as well as the Office of Naval Research (ONR GRANT #13330021). Funding from the National Science Foundation (DMR 1607922) for acquisition of the Q-smart pulsed laser system is gratefully acknowledged. Dr. Susheng Tan and Dr. Daniel Lamont are acknowledged for assistance with TEM imaging and TEM cross-sectional sample preparation. Kevin Byerly and Prof. Michael McHenry from Carnegie Mellon University are acknowledged for providing samples.

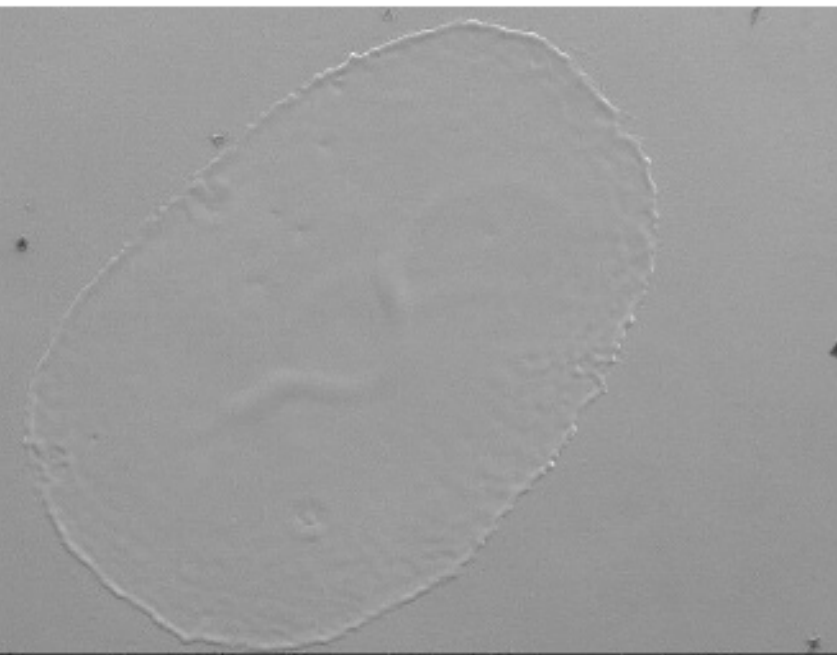
References

- ¹ M.E. McHenry and D.E. Laughlin, in *Phys. Metall. Fifth Ed.*, edited by D.E. Laughlin and K. Hono (Elsevier, Oxford, 2014), pp. 1881–2008.
- ² A. Talaat, D.W. Greve, M.V. Suraj, and P.R. Ohodnicki, *J. Alloys Compd.* **854**, 156480 (2021).
- ³ A. Talaat, M.V. Suraj, K. Byerly, A. Wang, Y. Wang, J.K. Lee, and P.R. Ohodnicki, *J. Alloys Compd.* **870**, 159500 (2021).
- ⁴ G. Herzer, *Acta Mater.* **61**, 718 (2013).
- ⁵ Y. Yoshizawa, S. Oguma, and K. Yamauchi, *J. Appl. Phys.* **64**, 6044 (1988).
- ⁶ K. Suzuki, R. Parsons, B. Zang, K. Onodera, H. Kishimoto, T. Shoji, and A. Kato, *AIP Adv.* **9**, 035311 (2019).
- ⁷ D. Azuma, N. Ito, and M. Ohta, *J. Magn. Magn. Mater.* **501**, 166373 (2020).
- ⁸ Y. Liu, M. Zheng, D.J. Sellmyer, and J. Mazumder, in *Handb. Adv. Magn. Mater.*, edited by Y. Liu, D.J. Sellmyer, and D. Shindo (Springer US, Boston, MA, 2006), pp. 1045–1063.
- ⁹ L. Lanotte and V. Iannotti, *J. Appl. Phys.* **78**, 3531 (1995).
- ¹⁰ S. Katakam, J.Y. Hwang, H. Vora, S.P. Harimkar, R. Banerjee, and N.B. Dahotre, *Scr. Mater.* **66**, 538 (2012).

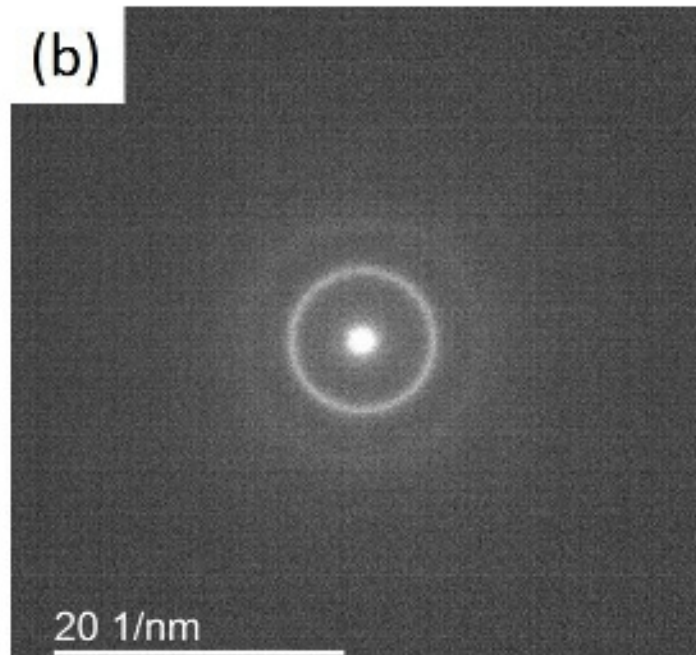
- ¹¹ A. Leary, V. Keylin, A. Devaraj, V. DeGeorge, P. Ohodnicki, and M.E. McHenry, *J. Mater. Res.* **31**, 3089 (2016).
- ¹² K. Byerly, P.R. Ohodnicki, S.R. Moon, A.M. Leary, V. Keylin, M.E. McHenry, S. Simizu, R. Beddingfield, Y. Yu, G. Feichter, R. Noebe, R. Bowman, and S. Bhattacharya, *JOM* **70**, 879 (2018).
- ¹³ M.A. McGuire and D.S. Parker, *J. Appl. Phys.* **118**, 163903 (2015).
- ¹⁴ B. Jayakumar and J.C. Hanan, in *Residual Stress Thermomechanics Infrared Imaging Hybrid Tech. Inverse Probl. Vol. 8*, edited by M. Rossi, M. Sasso, N. Connesson, R. Singh, A. DeWald, D. Backman, and P. Gloeckner (Springer International Publishing, Cham, 2014), pp. 87–92.
- ¹⁵ H.S. Chen, H.J. Leamy, and C.E. Miller, *Annu. Rev. Mater. Sci.* **10**, 363 (1980).
- ¹⁶ S.P. Harimkar, S.R. Paital, G. Wang, P.K. Liaw, and N.B. Dahotre, *Adv. Eng. Mater.* **13**, 955 (2011).
- ¹⁷ K. Tan, *IEEE Trans. Magn.* **22**, 188 (1986).
- ¹⁸ E.A. Theisen, M.J. Davis, S.J. Weinstein, and P.H. Steen, *Chem. Eng. Sci.* **65**, 3249 (2010).
- ¹⁹ W.J. Parker, R.J. Jenkins, C.P. Butler, and G.L. Abbott, *J. Appl. Phys.* **32**, 1679 (1961).
- ²⁰ M.A. Willard and M. Daniil, in *Handb. Magn. Mater.*, edited by K.H.J. Buschow (Elsevier, 2013), pp. 173–342.
- ²¹ P.R. Ohodnicki, D.E. Laughlin, M.E. McHenry, and M. Widom, *Acta Mater.* **58**, 4804 (2010).
- ²² U. Köster and U. Herold, in *Glas. Met. Ion. Struct. Electron. Transp. Cryst.*, edited by H.-J. Güntherodt and H. Beck (Springer Berlin Heidelberg, Berlin, Heidelberg, 1981), pp. 225–259.
- ²³ T. Kulik, *J. Non-Cryst. Solids* **287**, 145 (2001).
- ²⁴ U. Köster and J. Meinhardt, *Mater. Sci. Eng. A* **178**, 271 (1994).
- ²⁵ M.E. McHenry, F. Johnson, H. Okumura, T. Ohkubo, V.R.V. Ramanan, and D.E. Laughlin, *Scr. Mater.* **48**, 881 (2003).
- ²⁶ K. Suzuki, R. Parsons, B. Zang, K. Onodera, H. Kishimoto, T. Shoji, and A. Kato, *J. Alloys Compd.* **735**, 613 (2018).
- ²⁷ F. Alves, P. Houée, M. Lécivain, and F. Mazaleyrat, *J. Appl. Phys.* **81**, 4322 (1997).
- ²⁸ R.C. Hall, *J. Appl. Phys.* **30**, 816 (1959).



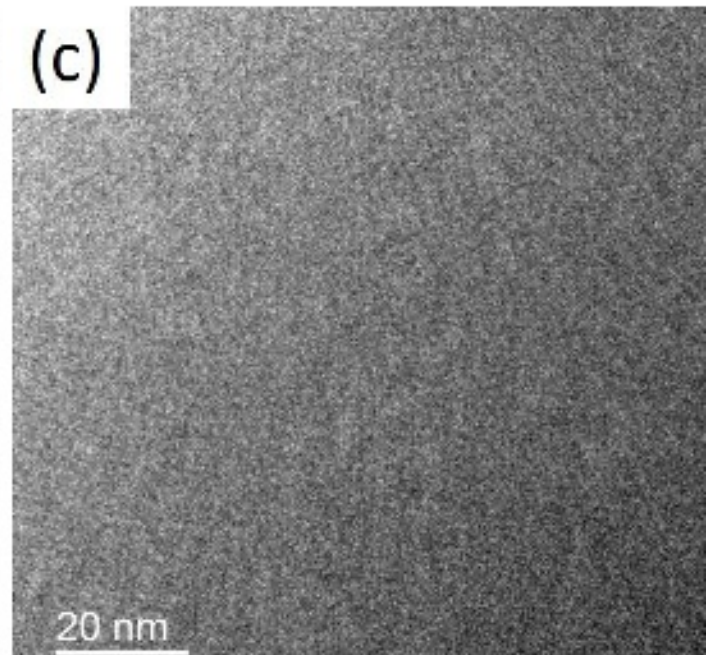
(a)

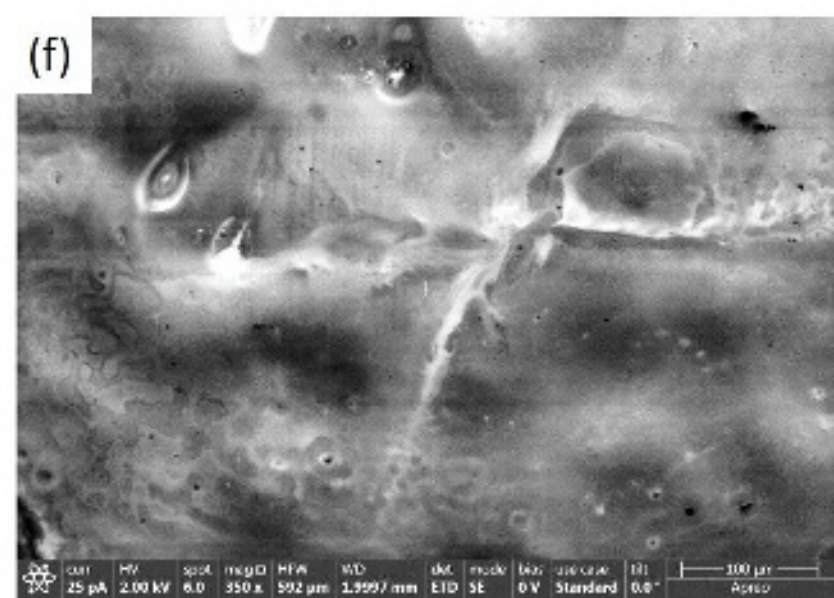
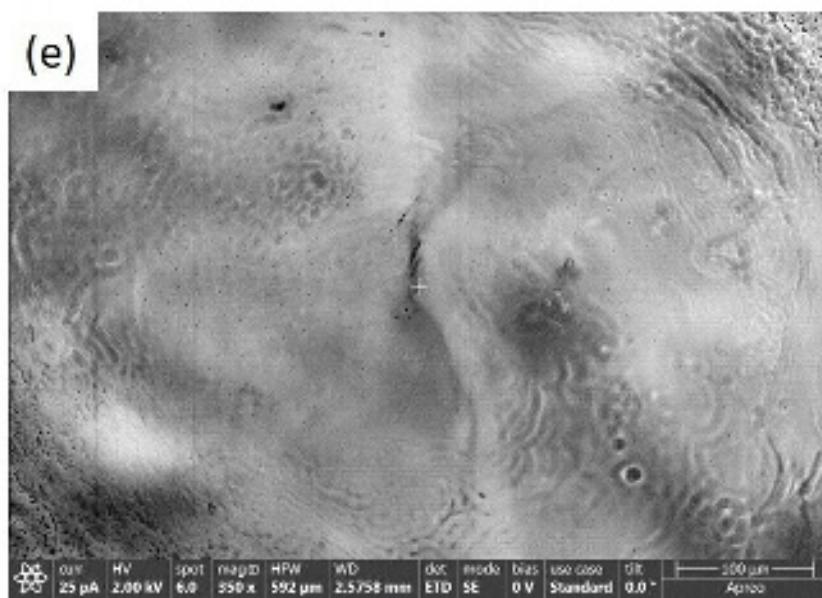
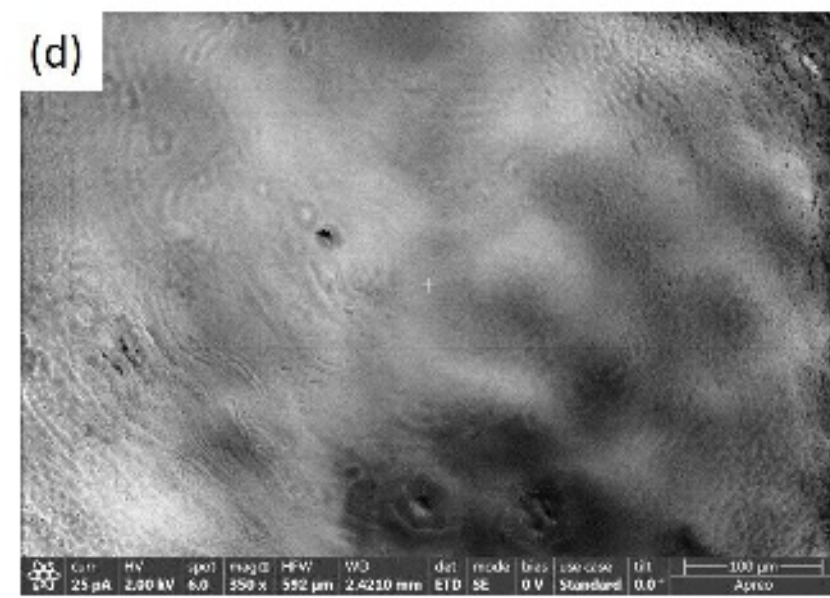
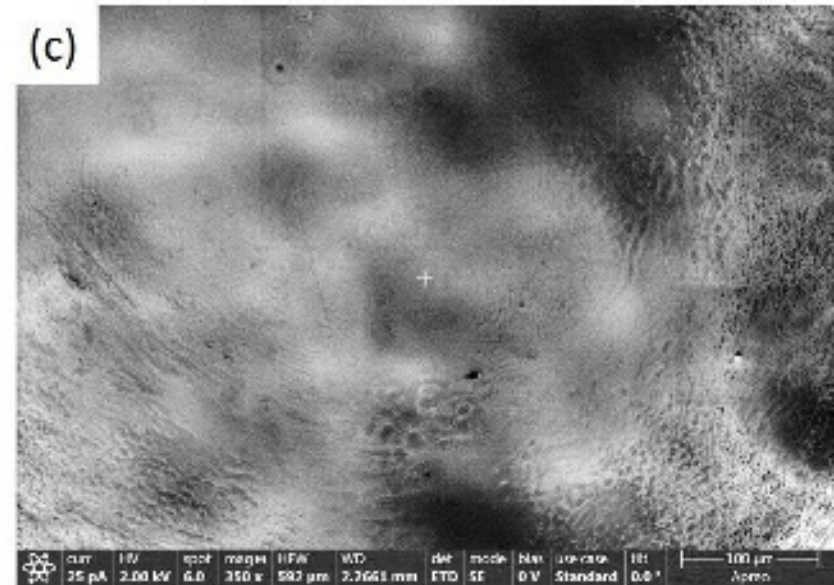
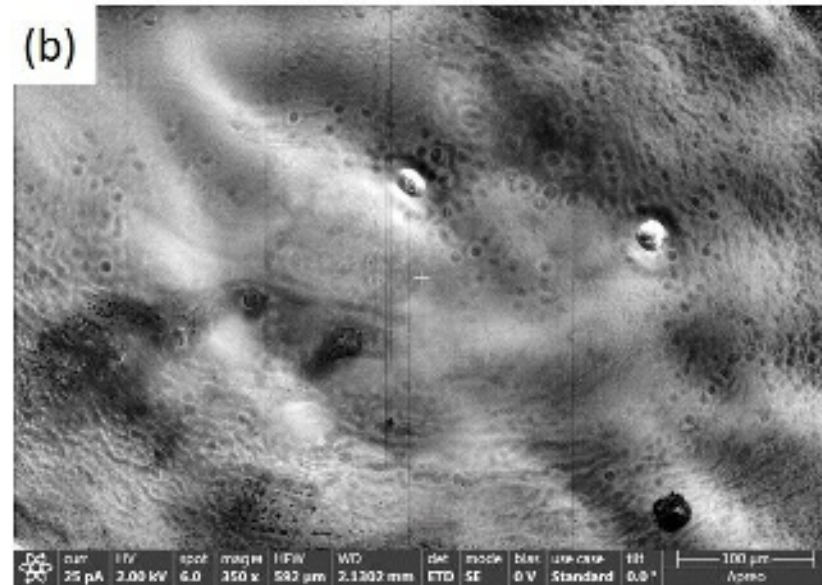
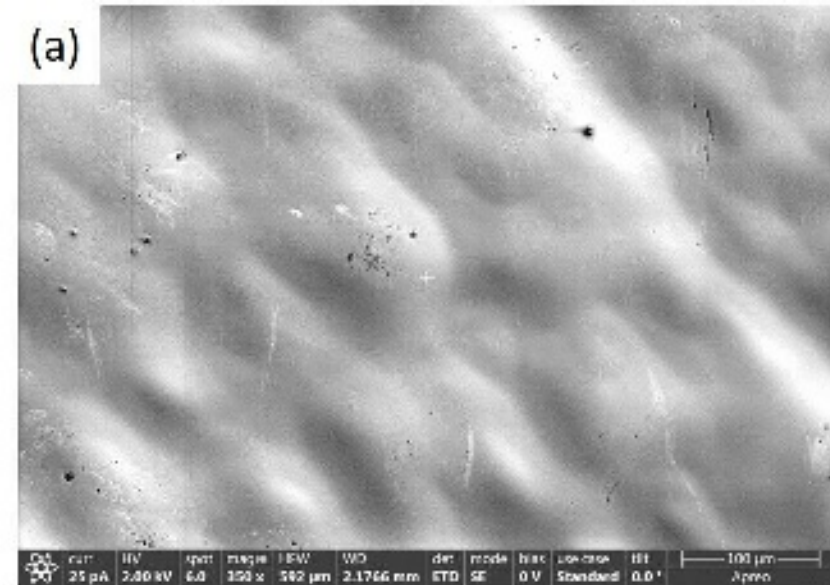


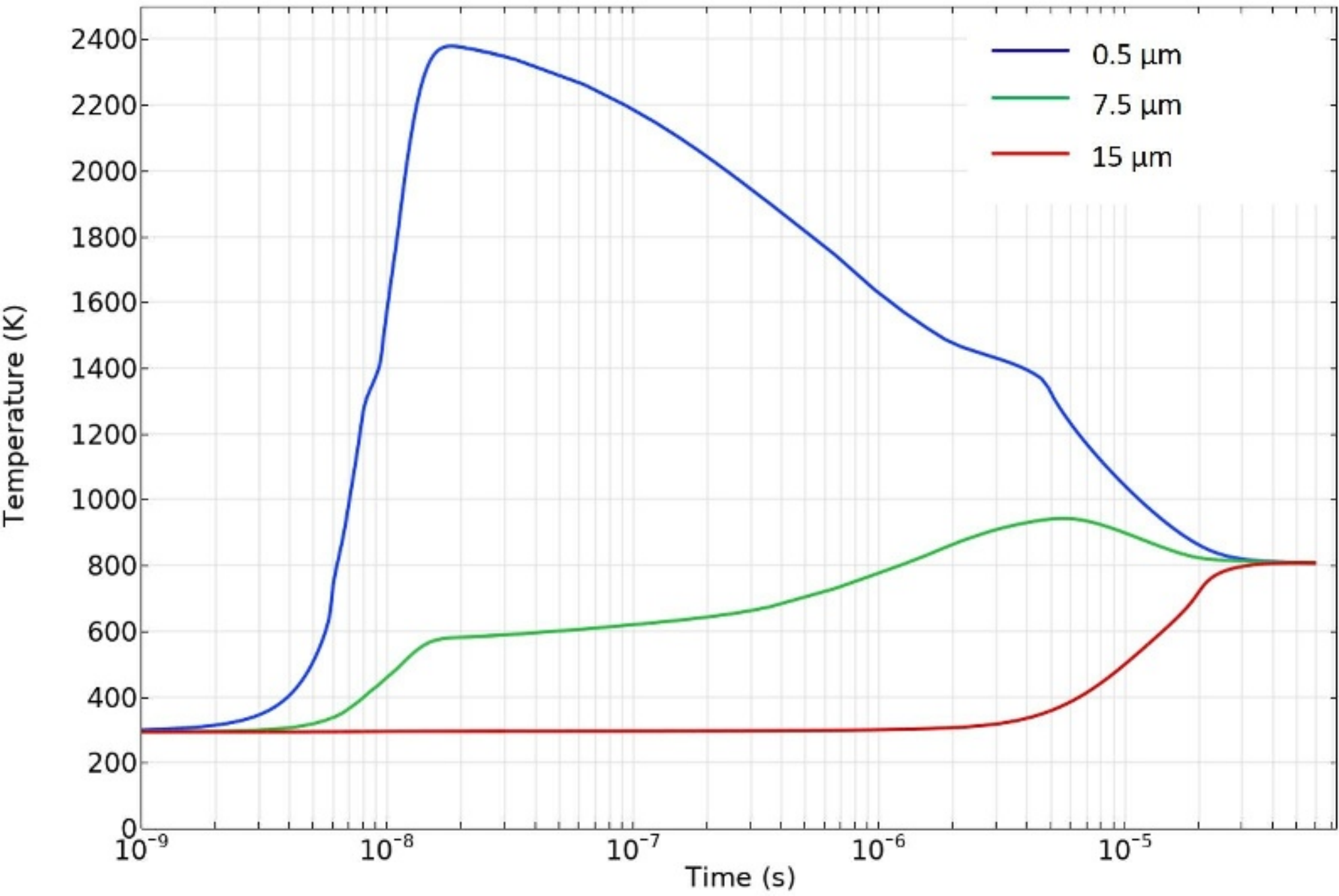
(b)



(c)







7.5 ns



1.0 μs



40 μs



10^{-3} m

$\times 10$

